Solution of incompressible fluid flow problems with heat transfer by means of an efficient RBF-FD meshless approach

R. Zamolo and E. Nobile

Department of Engineering and Architecture, University of Trieste, Trieste, Italy

ABSTRACT

The localized radial basis function collocation meshless method (LRBFCMM), also known as radial basis function generated finite differences (RBF-FD) meshless method, is employed to solve time-dependent, two-dimensional (2D) incompressible fluid flow problems with heat transfer using multiquadric RBFs. A projection approach is employed to decouple the continuity and momentum equations for which a fully implicit scheme is adopted for the time integration. The node distributions are characterized by non-Cartesian node arrangements and large sizes, i.e., in the order of 10^5 nodes, while nodal refinement is employed where large gradients are expected, i.e., near the walls. Particular attention is given to the accurate and efficient solution of unsteady flows at high Reynolds or Rayleigh numbers, in order to assess the capability of this specific meshless approach to deal with practical problems. Three benchmark test cases are considered: a lid-driven cavity, a differentially heated cavity and a flow past a circular cylinder between parallel walls. The obtained numerical results compare very favorably with literature references for each of the considered cases. It is concluded that the presented numerical approach can be employed for the efficient simulation of fluid-flow problems of engineering relevance over complex-shaped domains.

ARTICLE HISTORY

Accepted 4 February 2019

1. Introduction

The difficulties connected to the mesh, i.e., generation, properness, quality issues, and possible adaptation requirements, when using traditional mesh-based methods, led to the development of various meshless or meshfree methods for the solution of partial differential equations over complex-shaped domains encountered in practical problems [1] and [2]. Radial basis function (RBF) collocation approaches have been widely applied because of their real meshless nature [3]–[9], using both the global formulation [10] and the localized formulation [11]–[19]. The localized RBF collocation approach is also known as RBF-generated Finite Differences (RBF-FD) method because it is the extension of the standard FD schemes to irregular node arrangements using local RBF interpolants [20]. The coefficient matrix arising from such discretization is sparse, contrary to the full matrices arising from global approaches. Since sparse matrices are generally more efficient to solve and less prone to ill-conditioning than full matrices, the localized approaches have shown to be more efficient and robust compared to global approaches when a large number of nodes is employed [21]–[23]. In recent years such RBF-FD approach has been successfully employed for the solution of fluid flow and heat transfer problems [24]–[29], showing that this approach is very promising for the solution of practical problems of engineering relevance.

CONTACT R. Zamolo riccardo.zamolo@phd.units.it Department of Engineering and Architecture, University of Trieste, via Alfonso Valerio 10, 34127 Trieste, Italy.

Nomenclature

$\mathbf{B}$	nondimensional buoyancy vector	T_C	cold wall temperature
C_D	drag coefficient	T_H	hot wall temperature
d_{cyl}	cylinder diameter	u	Cartesian component of velocity
D_n	local support size	$\mathbf{u}$	velocity vector
D_T	energy equation parameter	$\mathbf{u}^*$	tentative velocity vector
D_u	momentum equation parameter	x	horizontal coordinate
e_W	spacing parameter, $e_W = 1.75$	$\hat{x}$	horizontal nodal coordinate
f	nondimensional frequency	$\mathbf{x}$	position vector
F_x	horizontal force	$\hat{\mathbf{x}}$	nodal positions
g	gravity acceleration	$\bar{\mathbf{x}}$	mean local support point
$\mathbf{g}$	gravity vector	y	vertical coordinate
i_{MAX}	number of nodes along x and y	Y	linear operator
$\mathbf{j}$	vertical unit vector	α	thermal diffusivity
J_n	local support	β	volumetric expansion coefficient
k_W	spacing parameter, $k_W = 3$	Δt	time step
k_C	spacing parameter, $k_C = 24$	ΔT	reference temperature scale
L	characteristic length	ε	shape factor
M	number of internal nodes	$\bar{\varepsilon}$	rescaled shape factor
M_D	number of Dirichlet nodes	γ	spacing parameter, $\gamma = 40$
M_N	number of Neumann nodes	Γ	boundary
n	number of local support nodes	Γ_N	Neumann boundary
$\mathbf{n}$	unit normal	ν	kinematic viscosity
Nu_y	local Nusselt number	Ω	domain
$\overline{\mathrm{Nu}}$	mean Nusselt number	ϕ	velocity correction potential
p	pressure	ψ	streamfunction
Pr	Prandtl number	ρ	density
Ra	Rayleigh number	***Subscripts***	
Re	Reynolds number	d	Cartesian component, $d = 1, 2$
s	spacing function	i, j	nodal indexes
s_m	minimum spacing function	k	iteration index
s_M	maximum spacing function	0	reference value
t	time	***Superscripts***	
$\bar{t}$	shedding period	n	time level
T	temperature		

This article is intended to continue and extend the application of the RBF-FD method to two-dimensional incompressible fluid flow problems with heat transfer for which important practical issues are addressed, such as the use of irregular node arrangements with variable nodal spacing, an efficient solution procedure for large size problems with approximately 10^5 nodes or more, the possibility to deal with moderately high Reynolds (Re) or Rayleigh (Ra) numbers and the use of primitive flow variables, i.e., velocity and pressure. The use of irregular node arrangements with variable nodal spacing has two practical outcomes: the possibility to deal with arbitrarily-shaped domains, which is one of the strengths of meshless methods, and the opportunity to employ high node density, i.e., small nodal spacing, where large gradients are expected, similarly to traditional mesh based methods. Computational efficiency is achieved by coupling a projection scheme [29] with a fully implicit scheme for the momentum equations, which allows the use of large time steps and therefore providing an effective time integration procedure. A compact local support for the RBF discretization is employed, i.e., $n = 7$ nodes, allowing an efficient iterative process at each time step, for which the fast solution of large and sparse linear systems is of utmost importance. Finally, the employment of a primitive variables formulation allows a straightforward extension to three-dimensional problems with possible applications to more complex fluid flow phenomena.

The developed RBF-FD meshless scheme is applied here to the solution of three classic benchmark problems: a lid-driven cavity at Re = 1,000, 5,000, 7,500, 10,000, a differentially heated cavity at Ra = 10^6, 10^7, 10^8, $2 \times 10^8, 4 \times 10^8$, and a flow past a circular cylinder between parallel walls at Re = 200, 300, 500, 1,000, 2,000, 4,000, 8,000. For each of these problems, suitable node distributions are easily generated starting from a simple spacing function definition in order to get higher node density where needed, e.g., near the walls. Very good results have been obtained for each of these test cases in terms of both quantitative numerical results and computational efficiency, showing the capability of the proposed method to deal with steady and unsteady flows at high Re or Ra numbers. Alongside the typical implementation ease of meshless methods, these features confirm that the present RBF-FD approach can be effectively used for the simulation of fluid-flow problems with heat transfer over complex-shaped domains with possible time-dependent behavior. Furthermore, the possibility of a straightforward extension to three-dimensional problems is an important feature when facing engineering relevant problems.

2. Governing equations

A two-dimensional, incompressible and nonisothermal flow is considered, for which the conservation equations of mass, momentum and energy are the following:

$$\nabla \cdot \mathbf{u} = 0 \tag{1}$$

$$\frac{\partial \mathbf{u}}{\partial t} + (\mathbf{u} \cdot \nabla)\mathbf{u} = -\frac{1}{\rho_0}\nabla p + \nu \nabla^2 \mathbf{u} - \mathbf{g}\beta(T - T_0) \tag{2}$$

$$\frac{\partial T}{\partial t} + \mathbf{u} \cdot \nabla T = \alpha \nabla^2 T \tag{3}$$

where the pressure p is deprived of the hydrostatic component and the Boussinesq approximation is employed, i.e., constant thermophysical properties except for the density in the buoyancy term which has a linearized dependence on the temperature:

$$\frac{\rho}{\rho_0} = -\beta(T - T_0) \tag{4}$$

where T_0 and ρ_0 are the reference values for temperature and density in the linearization, respectively. In the case of isothermal flows, the energy Eq. (3) is not considered and the buoyancy term is dropped, i.e., $\beta = 0$.

Eqs. (1)–(3) can be made nondimensional using the following reference values: L for length, u_0 for velocities, L/u_0 for time, ΔT for temperature, and $\rho_0 u_0^2$ for pressure. For isothermal flows, the flow Reynolds number is defined as $\mathrm{Re} = u_0 L/\nu$, while for nonisothermal flows the Rayleigh number $\mathrm{Ra} = g\beta\Delta T L^3/(\nu\alpha) = u_0^2 L^2/(\nu\alpha)$ and the Prandtl number $\mathrm{Pr} = \nu/\alpha$ are chosen as nondimensional groups. A Prandtl number $Pr = 0.71$ is chosen, which is representative of air. The nondimensional form of Eqs. (1)–(3) is therefore:

$$\nabla \cdot \mathbf{u} = 0 \tag{5}$$

$$\frac{\partial \mathbf{u}}{\partial t} + (\mathbf{u} \cdot \nabla)\mathbf{u} = -\nabla p + \frac{1}{D_u}\nabla^2 \mathbf{u} + \mathbf{B} \tag{6}$$

$$\frac{\partial T}{\partial t} + \mathbf{u} \cdot \nabla T = \frac{1}{D_T}\nabla^2 T \tag{7}$$

where $\mathbf{B} = (T - T_0)\mathbf{j}$ in the non-isothermal cases; T_0 is assumed to be 0 without loss of generality. The values for D_u, D_T, and $\mathbf{B}$ are reported in Table 1 for isothermal and nonisothermal cases.

Table 1. Parameters for Eqs. (6) and (7) for isothermal and nonisothermal cases

Case	D_u	D_T	B
Isothermal	Re	–	0
Nonisothermal	$\sqrt{\mathrm{Ra}/\mathrm{Pr}}$	$\sqrt{\mathrm{RaPr}}$	$T\mathbf{j}$

3. Numerical procedure

3.1. Time discretization and solution procedure

A second order backward Euler scheme, or Gear scheme, is employed for the time discretization of Eqs. (6)–(7), while a segregated approach is chosen for the decoupling of the system of Eqs. (5)–(7). The projection approach [29] is employed for the decoupling of mass and momentum equations. At each iteration k the tentative velocity $\mathbf{u}^*$ is computed by implicitly solving the momentum Eq. (6) with a linearized advective (nonlinear) term as follows:

$$\frac{3\mathbf{u}_k^*}{2\Delta t} + \mathbf{u}_{k-1}^{n+1}\nabla\mathbf{u}_k^* - \frac{1}{D_u}\nabla^2\mathbf{u}_k^* = \frac{4\mathbf{u}^n - \mathbf{u}^{n-1}}{2\Delta t} - \nabla p_{k-1}^{n+1} + \mathbf{B}_{k-1}^{n+1} \tag{8}$$

where the values with iteration index k – 1 are extrapolated at the first iteration $k=1$ as follows: $\mathbf{u}_0^{n+1} = 2\mathbf{u}^n - \mathbf{u}^{n-1}, \mathbf{B}_0^{n+1} = 2\mathbf{B}^n - \mathbf{B}^{n-1}, p_0^{n+1} = \frac{3}{2}p^n - \frac{1}{2}p^{n-1}$.

The tentative velocity $\mathbf{u}_k^*$ is then projected onto the space of divergence-free fields in order to satisfy the continuity Eq. (5) [29], i.e., $\mathbf{u}_k^*$ is deprived from its irrotational component $\nabla\phi$:

$$\mathbf{u}_k^{n+1} = \mathbf{u}_k^* - \nabla\phi \tag{9}$$

The equation for the potential ϕ is obtained by taking the divergence of Eq. (9) and enforcing the mass constraint $\nabla\cdot\mathbf{u}_k^{n+1} = 0$, obtaining the following Poisson equation:

$$\nabla^2\phi = \nabla\cdot\mathbf{u}_k^* \tag{10}$$

subject to the boundary condition $\nabla\phi\cdot\mathbf{n} = 0$ on the whole boundary in order to satisfy the normal boundary condition for the velocities. Poisson Eq. (10) has to be solved at each time step in order to compute the velocity correction of Eq. (9).

The pressure is then updated as:

$$p_k^{n+1} = p_{k-1}^{n+1} + \frac{3\phi}{2\Delta t} \tag{11}$$

Lastly, the temperature is computed by implicitly solving the energy Eq. (7) for T_k^{n+1} :

$$\frac{3T_k^{n+1}}{2\Delta t} + \mathbf{u}_k^{n+1}\nabla T_k^{n+1} - \frac{1}{D_T}\nabla^2 T_k^{n+1} = \frac{4T^n - T^{n-1}}{2\Delta t} \tag{12}$$

where the divergence-free velocity $\mathbf{u}_k^{n+1}$ is now considered for the advective term.

The whole system of Eqs. (8)–(12) is iterated four times for each time step in order to properly address the nonlinear coupling between the different variables, especially when using large time-steps.

Since implicit solvers are employed for both the computation of velocities, Eq. (8), and temperature, Eq. (12), there is no stability requirement for the choice of the time step Δt, i.e., CFL condition, and therefore it is possible to employ large time steps, i.e., large Courant numbers $C = \Delta t||\mathbf{u}||/s \gg 1$ where s is the nodal spacing, allowing an efficient time marching scheme.

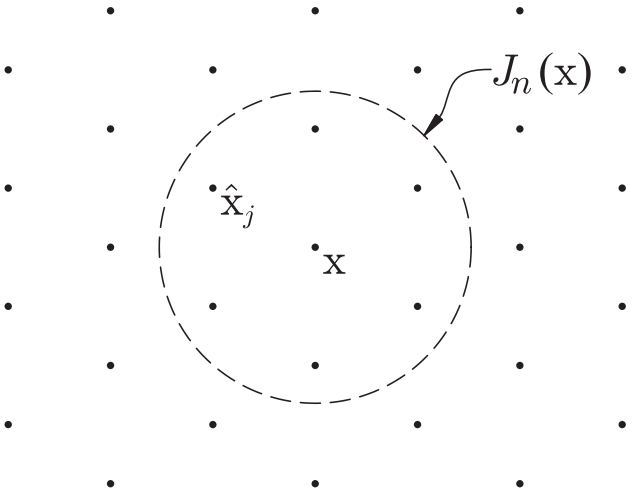

Figure 1. Example of a local support for the RBF expansion around **x**. The nodes $\hat{\mathbf{x}}_j$ inside the circle are the 7 nearest nodes from **x**.

3.2. RBF-FD space discretization

3.2.1. 2D Node distributions

The RBF-FD meshless approach requires a set of N nodes $\hat{\mathbf{x}}_i,\ i = 1, ..., N$, appropriately distributed over the domain and its boundary. M nodes are distributed inside the domain Ω (internal nodes), while the remaining $N - M$ nodes are distributed over the boundary Γ (boundary nodes). Boundary nodes are composed by M_D Dirichlet nodes, i.e., where Dirichlet BCs are imposed, and $M_N = N-M-M_D$ Neumann nodes, i.e., where Neumann BCs are imposed. Such two-dimensional node distributions have been obtained through the technique proposed in [30] in the case of isothermal problems where isotropic node arrangements are required. This node generation technique employs a modified quadtree algorithm followed by repel refinement in order to obtain high quality node distributions; such algorithm is briefly summarized here.

Starting from a prescribed spacing function $s(\mathbf{x})$, which defines the spacing between the nodes, an initial node distribution is obtained through the quadtree algorithm [31] modified with a dithering correction [32] in order to reduce the nodal quantization error, i.e., the difference between the integer number of nodes that can be contained in any square box Ω and the prescribed (non-integer) node number $\int_\Omega s(\mathbf{x})^{-2} \mathrm{d}\omega$. The resulting node distribution is then improved by the application of a certain number of refinement iterations which are based on radial repel forces between the nodes, while a fixed boundary distribution of nodes is employed (Figure 1).

In the case of the differentially heated cavity, the employment of anisotropic node distributions is required for the efficient and accurate solution of the thin boundary layer occurring at the vertical walls. In such cases we employed Cartesian nodal arrangements which are highly stretched near the walls of the cavity.

3.2.2. Localized RBF interpolation

A localized RBF expansion augmented with a linear polynomial is employed to approximate a generic field ξ in the neighborhood of **x**:

$$\xi(\mathbf{x}) = \sum_{j \in J_n(\mathbf{x})} a_j \varphi\left(\|\mathbf{x} - \hat{\mathbf{x}}_j\|\right) + \mathbf{b}^T(\mathbf{x}-\bar{\mathbf{x}}) + c \tag{13}$$

where $J_n(\mathbf{x})$ is the set of the indices j of the n nodes $\hat{\mathbf{x}}_j$ closest to $\mathbf{x} = \{x_1, x_2\}^T$. Such local nodes represent the local support for $\xi(\mathbf{x})$ and $\bar{\mathbf{x}} = \sum_{j \in J_n(\mathbf{x})} \hat{\mathbf{x}}_j / n$ is the mean point for the local support.

When isotropic distributions are employed, we used $n=7$ local nodes, since this choice allows a second order accuracy and the higher fraction of positive stencils in the range $n<10$ [30], in the case of the Poisson Eq. (10). In the case of Cartesian node arrangements, the traditional five-point stencil is employed, i.e., $n=5$.

The expansion defined by Eq. (13) is therefore a linear combination of n radial functions φ centered at the n local nodes $\hat{\mathbf{x}}_j$ plus a linear polynomial in $\mathbf{x}$. The choice of a linear polynomial follows the recommendation $2q \lesssim n = 5 \div 7$ [33], where q is the number of polynomial terms, therefore $q=3$ is the higher number of allowed polynomial terms, corresponding to a complete linear polynomial in 2D.

Hardy's multiquadric (MQ) [34] is chosen as RBF since it seems to offer the best interpolation results if an appropriate shape factor ε is employed [35] and [36]:

$$\varphi(r) = \sqrt{1 + (\varepsilon r)^2} \tag{14}$$

In Eq. (14) the shape factor ε is rescaled as:

$$\varepsilon = s_M \bar{\varepsilon} / D_n(\mathbf{x}) \tag{15}$$

where $\bar{\varepsilon}$ is the rescaled shape factor, s_M is the maximum prescribed spacing function over the domain and $D_n(\mathbf{x})$ is the local support size:

$$D_n(\mathbf{x}) = \sqrt{\frac{1}{n} \sum_{j \in J_n(\mathbf{x})} \|\hat{\mathbf{x}}_j - \bar{\mathbf{x}}\|^2} \tag{16}$$

The rescaling defined by Eq. (15) is motivated by two reasons. The first reason is to avoid large differences in the condition number for the local interpolation matrix of Eq. (20) between different parts of the domain where different nodal spacings are employed, while the second reason is to avoid the appearance of stagnation errors [37] when nodal spacing is continuously reduced on the whole domain. The former issue is addressed by dividing $\bar{\varepsilon}$ by the local support size $D_n(\mathbf{x})$, while the latter issue is addressed by multiplying $\bar{\varepsilon}$ by the maximum prescribed spacing function over the domain s_M. Obviously, the rescaled shape factor $\bar{\varepsilon}$ has to be chosen in order to avoid ill-conditioned local interpolation matrices. In all the presented results a rescaled shape factor $\bar{\varepsilon} = 1$ is employed.

The coefficients a_j, $\mathbf{b}$, and c in Eq. (13) are formally obtained by writing the same Eq. (13) for the $m \leq n$ local nodes $\hat{\mathbf{x}}_i$ which do not lie on the part of the boundary Γ where Neumann BCs are imposed (Neumann boundary Γ_N):

$$\sum_{j \in J_n(\mathbf{x})} a_j \varphi\left(\|\hat{\mathbf{x}}_i - \hat{\mathbf{x}}_j\|\right) + \mathbf{b}^T(\hat{\mathbf{x}}_i - \bar{\mathbf{x}}) + c = \xi_i \qquad i \in I_n(\mathbf{x}) \tag{17}$$

where ξ_i is the value for ξ in $\hat{\mathbf{x}}_i$ and $I_n(\mathbf{x}) \subseteq J_n(\mathbf{x})$ is the set of the indices i of the $m \leq n$ local nodes $\hat{\mathbf{x}}_i$ which do not lie on the Neumann boundary Γ_N. It is appropriate to require exactness of Eq. (13) for any linear function ξ: Eq. (17) with $\xi_i = \mathbf{b}^T \hat{\mathbf{x}}_i + c$ should give the unique obvious solution $a_j = 0$. Since the MQ-RBF interpolation matrix is always invertible [38], any additional homogeneous linear system in a_j with rank 3 can be employed. It is then convenient to impose the following homogeneous conditions in order to get a symmetric interpolation matrix:

$$\sum_{j \in J_n(\mathbf{x})} a_j = 0, \qquad \sum_{j \in J_n(\mathbf{x})} a_j (\hat{\mathbf{x}}_j - \bar{\mathbf{x}}) = 0 \tag{18}$$

If a local support node $\hat{\mathbf{x}}_k$ lies on a Neumann boundary Γ_N, $\hat{\mathbf{x}}_k$ is a Neumann node and the corresponding boundary condition has to be satisfied:

$$\left.\frac{\partial \xi}{\partial \mathbf{n}}\right|_{\hat{\mathbf{x}}_k} = \sum_{j \in J_n(\mathbf{x})} a_j \frac{\partial}{\partial \mathbf{n}} \left[\varphi\left(\|\mathbf{x} - \hat{\mathbf{x}}_j\|\right)\right]_{\hat{\mathbf{x}}_k} + \mathbf{b}^T \mathbf{n} = \bar{\xi}_k \qquad k \in K_n(\mathbf{x}) \tag{19}$$

where $\bar{\xi}_k$ is the imposed outward normal derivative for ξ on the Neumann node $\hat{\mathbf{x}}_k$, $\mathbf{n}$ is the unit outward normal to the boundary in $\hat{\mathbf{x}}_k$ and $K_n(\mathbf{x}) \subset J_n(\mathbf{x})$ is the set of the indices k of the $n - m$ local nodes $\hat{\mathbf{x}}_k$ lying on the Neumann boundary Γ_N. $I_n(\mathbf{x})$ and $K_n(\mathbf{x})$ are disjoint sets and $J_n(\mathbf{x}) = I_n(\mathbf{x}) \cup K_n(\mathbf{x})$.

By collecting n local coefficients a_j, m unknown values ξ_i and $n - m$ normal derivatives $\bar{\xi}_k$ in column vectors $\mathbf{a}$, $\boldsymbol{\xi}_{loc}$ and $\bar{\boldsymbol{\xi}}_{loc}$, respectively, the local interpolation system is:

$$\mathbf{G}\mathbf{e} = \boldsymbol{\xi}'_{loc} \tag{20}$$

where $\mathbf{e} = \{\mathbf{a}; \mathbf{b}; c\} \in \mathbb{R}^{n+3}$ is the column vector of RBF expansion coefficients, $\boldsymbol{\xi}'_{loc} = \{\boldsymbol{\xi}_{loc}; 0; \bar{\boldsymbol{\xi}}_{loc}\} \in \mathbb{R}^{n+3}$ is the column vector of local nodal values and outward normal derivatives (the symbol ';' denotes column concatenation) and the zero vector is a column vector with three components corresponding to the three conditions of Eq. (18). $\mathbf{G}$ is a square $(n+3) \times (n+3)$ matrix whose first $(m+3)$ rows represent the contribution of MQ-RBF interpolation with an augmented linear polynomial as expressed by Eq. (13), while the remaining $(n-m)$ rows represent the equations for Neumann BCs, if any. If $m = n$, i.e., no local support nodes on the Neumann boundary, an LDL^T factorization is performed on $\mathbf{G}$ since it is symmetric but not positive definite, otherwise a Schur complement [39] is first performed for the Neumann equations, followed again by an LDL^T factorization on the remaining symmetric part of $\mathbf{G}$.

It is convenient to introduce the following compact form for the RBF expansion of Eq. (13):

$$\xi(\mathbf{x}) = \boldsymbol{\psi}(\mathbf{x})\mathbf{e} \tag{21}$$

where $\boldsymbol{\psi}(\mathbf{x}) = \{\varphi(\|\mathbf{x} - \hat{\mathbf{x}}_1\|), \ldots, \varphi(\|\mathbf{x} - \hat{\mathbf{x}}_n\|), (\mathbf{x}-\bar{\mathbf{x}})^T, 1\}$ is the row vector of RBFs, including the polynomial terms.

3.2.3. RBF-FD approach

Let us consider the following linear PDE:

$$Y(\xi) = q \tag{22}$$

where Y is a linear differential operator and q is a known function. Recalling the compact notation of Eq. (21) for ξ, Eq. (22) is made valid on each of the M internal nodes $\hat{\mathbf{x}}_i$ through the collocation approach:

$$Y(\boldsymbol{\psi}(\mathbf{x}))|_{\hat{\mathbf{x}}_i}\mathbf{e} = q(\hat{\mathbf{x}}_i) \qquad i = 1, \ldots, M \tag{23}$$

where $Y(\boldsymbol{\psi}(\mathbf{x}))|_{\hat{\mathbf{x}}_i}$ is obtained by applying the differential operator Y to each scalar function composing the vector $\boldsymbol{\psi}(\mathbf{x})$, evaluated at the collocation node $\hat{\mathbf{x}}_i$, while $\mathbf{e}$ is moved outside Y because of its linearity.

By recalling $\mathbf{e} = \mathbf{G}^{-1}\boldsymbol{\xi}'_{loc}$ from Eq. (20), Eq. (23) becomes:

$$Y(\boldsymbol{\psi}(\mathbf{x}))|_{\hat{\mathbf{x}}_i}\mathbf{G}^{-1}\boldsymbol{\xi}'_{loc} = q(\hat{\mathbf{x}}_i) \qquad i = 1, \ldots, M \tag{24}$$

Eq. (24) therefore represents the final RBF-FD equation for the M internal nodes $\hat{\mathbf{x}}_i$. The RBF-FD definition is due to the fact that Eq. (24) represents a pointwise, or collocation, approximation of the starting differential Eq. (22) using local nodal values for the unknown function. The first m components of row vector $Y(\boldsymbol{\psi}(\mathbf{x}))|_{\hat{\mathbf{x}}_i}\mathbf{G}^{-1}$ define the stencil, i.e., the equation coefficients for $\boldsymbol{\xi}'_{loc}$, while the remaining $n - m$ components define the coefficients for the imposed outward normal derivatives on ξ for Neumann local nodes, if any.

Writing Eq. (24) for each internal node $\hat{\mathbf{x}}_i$, $i = 1, \ldots, M$, gives the following linear system:

$$\mathbf{A}\boldsymbol{\xi} + \bar{\mathbf{A}}\bar{\boldsymbol{\xi}} = \mathbf{q} \tag{25}$$

where $\boldsymbol{\xi} \in \mathbb{R}^{M+M_D}$ is the column vector of ξ values for all M internal nodes and M_D Dirichlet nodes, while $\bar{\boldsymbol{\xi}} \in \mathbb{R}^{M_N}$ is the column vector of imposed outward normal derivatives on ξ for M_N

Neumann nodes. $\mathbf{A} \in \mathbb{R}^{M\times(M+M_D)}$ and $\bar{\mathbf{A}} \in \mathbb{R}^{M\times M_N}$ are the corresponding coefficient matrices and $\mathbf{q} \in \mathbb{R}^M$ is the column vector of RHS terms $q(\hat{\mathbf{x}}_i)$ for each of the M internal nodes.

The order of the entries in the column vector $\boldsymbol{\xi}$ is chosen to have the unknown values at the internal nodes at the beginning, followed by the known values at the Dirichlet nodes. This is formally expressed by $\boldsymbol{\xi} = \{\boldsymbol{\xi}_I; \boldsymbol{\xi}_D\}$, where the subscripts I and D stand for internal and Dirichlet nodes, respectively. Eq. (25) then becomes:

$$\mathbf{A}_I\boldsymbol{\xi}_I = \mathbf{q} - \bar{\mathbf{A}}\bar{\boldsymbol{\xi}} - \mathbf{A}_D\boldsymbol{\xi}_D \tag{26}$$

where $\mathbf{A}_I \in \mathbb{R}^{M\times M}$ and $\mathbf{A}_D \in \mathbb{R}^{M\times M_D}$ are the coefficient matrices for internal and Dirichlet nodes, respectively, and are obtained as a column partition of $\mathbf{A}$ following the corresponding ordering for $\boldsymbol{\xi}$: $\mathbf{A} = [\mathbf{A}_I\mathbf{A}_D]$.

Eq. (26) is the final $M \times M$ sparse linear system representing the discretized version of Eq. (22). Eq. (22) solved for $\boldsymbol{\xi}_I$ gives the nodal values for ξ on the M internal nodes.

3.2.4. RBF-FD for the momentum equation

Each scalar component of the linearized momentum Eq. (8), in a Cartesian coordinate system, can be recast in the form of Eq. (22) where the linear differential operator Y is given by:

$$Y(\xi) = \frac{3\xi}{2\Delta t} + \mathbf{u}^{n+1}\nabla\xi - \frac{1}{D_u}\nabla^2\xi \tag{27}$$

where $\xi = u_d^*,\ d = 1, 2$ for each of the Cartesian components of the tentative velocity $\mathbf{u}^* = \{u_1^*, u_2^*\}^T$ and the iteration subscript k is dropped for simplicity of notation. The RHS function q is given by the RHS of Eq. (8):

$$q = \frac{4u_d^n - u_d^{n-1}}{2\Delta t} - \frac{\partial p^{n+1}}{\partial x_d} + B_d^{n+1} \qquad d = 1, 2 \tag{28}$$

where $\mathbf{u} = \{u_1, u_2\}^T, \mathbf{B} = \{B_1, B_2\}^T$ in Cartesian components and the iteration subscript k is again dropped. Since the advective term in Eq. (8) is linearized, each of its Cartesian components can be solved independently for $u_d^*,\ d = 1, 2$.

3.2.5. RBF-FD for the Poisson equation and velocity correction

Poisson Eq. (10) is already in the form of Eq. (22) with $Y = \nabla^2$ and $q = \nabla \cdot \mathbf{u}_k^*$. The divergence term for q is approximated applying the same RBF-FD scheme employed for the discretization. When the discretized Poisson equation is solved for the potential ϕ on the internal nodes, it is possible to correct the nodal tentative velocities $\mathbf{u}_k^*$ using the correction Eq. (9) where the gradient operator is again approximated using the same RBF-FD scheme employed for the discretization of the Poisson equation.

It is important to notice that the present approach for the velocity correction does not satisfy exactly the continuity Eq. (1) at discrete level, i.e., the discrete divergence of the corrected velocity evaluated with the present RBF-FD scheme is not exactly 0 even if the discretized Poisson equation is solved at machine zero. This is due to the RBF-FD discretization of the Poisson Eq. (10), for which the incompressibility constraint, i.e., vanishing divergence for velocity, is imposed before the discretization. Although this approach introduces a certain amount of numerical mass generation/elimination, it is found to be much more stable and efficient than trying to impose a perfect satisfaction of the discretized continuity equation. In fact, this last operation consists in a double application of a discrete RBF-FD differential operator (gradient followed by divergence) to the potential of Eq. (9), which implies a stencil which is almost three times larger than the compact stencil employed for the Poisson equation (19 nodes *vs.* 7 nodes for a hexagonal node arrangement).

Another important observation concerns the treatment of the pressure p in the momentum equations and in the pressure update after the solution for the potential ϕ. It is known that the velocity-pressure coupling in discrete formulations can give rise to spurious/checkerboarding pressure modes if the same discretization scheme is employed for both quantities [40]. In the present formulation, this issue is addressed by considering an additional node distribution for the pressure, which has twice the spacing of the starting node distributions, therefore having roughly $N/4$ nodes in 2D. The potential ϕ is still solved on the original node distribution and is also used for the velocity correction, Eq. (9), on the same node distribution, but ϕ is then interpolated onto the coarse node distribution for the pressure update, Eq. (11), and for the calculation of pressure gradient in Eq. (28).

3.2.6. RBF-FD for the energy equation

The energy Eq. (12) can be recast in the form of Eq. (22) where the linear differential operator Y is given by:

$$Y(\xi) = \frac{3\xi}{2\Delta t} + \mathbf{u}^{n+1}\nabla\xi - \frac{1}{D_T}\nabla^2\xi \tag{29}$$

where $\xi = T$, while the RHS function q is given by the RHS of Eq. (12):

$$q = \frac{4T^n - T^{n-1}}{2\Delta t} \tag{30}$$

3.3. Solution techniques

The application of the previously introduced RBF-FD discretization to Eqs. (8), (10), and (12) leads to a large and sparse linear system for each of the corresponding scalar equations. Therefore, four formally independent linear systems have to be solved at each iteration k within each time step, in the following order: two linear systems for the momentum equations, one linear system for the Poisson equation and one linear system for the energy equation.

The RBF-FD coefficient matrix for the Poisson Eq. (10) is constant at each time step since it is time-independent. Therefore, it is convenient to perform a single LU factorization for this matrix at the beginning of the simulation and use it at each time step for the calculation of the potential ϕ, allowing a very fast and accurate solution. In the case of cavities, the Poisson equation is undetermined up to a constant and the uniqueness of the solution is obtained by using a Lagrange multiplier.

The RBF-FD coefficient matrices for momentum and energy Eqs. (8), (12) are time-dependent because of the advection term which depends upon the velocity, therefore the previous LU approach cannot be used. An efficient solution strategy is obtained by employing the BiCGSTAB iterative solver [41] with an incomplete LU (ILU) factorization [42] as preconditioner and reverse Cuthill–McKee ordering [43]. The ILU factorization is performed each $1 \div 2$ time steps during the transient, i.e., starting from resting fluid or restarting from a previous solution at lower Re/Ra, as well as for time-dependent flows with strong recirculations, i.e., the flow past the cylinder and the lid-driven cavity at high Re. The ILU factorization is performed less frequently when a solution is approaching the steady-state (factorization every $25 \div 50$ time steps) or in the case of the differentially heated cavity where most of the fluid is at rest even for time-dependent solutions (factorization every $10 \div 20$ time steps).

In the case of a ILU factorization at each time step, it is very important to choose a suitable ILU drop tolerance in order to minimize the overall time required for the ILU factorization and the BiCGSTAB solution at each time step. Low ILU drop tolerances involve high ILU

factorization times and low BiCGSTAB solution times for each time step, and vice versa. Therefore there exists an optimal ILU drop tolerance which minimizes the overall solution time per time step. Such value, which depends upon the matrix nature, residual tolerance for the iterative solution and hardware/implementation characteristics, is continuously and automatically optimized during the simulation by a simple optimization cycle. The residual relative tolerance for BiCGSTAB is set to 10^{-8} for the velocities and 10^{-11} for the temperature, for which two to four BiCGSTAB iterations are typically required. With these choices, the typical computing time on a quad-core Intel® i7 2.6GHz laptop with a MATLAB implementation is $1.2 \div 2.0$ s/(time step) when $N \approx 10^5$ nodes are employed.

3.3.1. Auxiliary computations

The calculation of the streamfunction ψ, required for vortices detection and graphical evaluation of the flow features, is carried out by solving the following Poisson equation:

$$\nabla^2 \psi = -\nabla \times \mathbf{u} \tag{31}$$

subject to the boundary condition $\psi = \bar{\psi}$. The boundary streamfunction $\bar{\psi}$ is constant at all solid walls, while $\bar{\psi}$ is obtained from the imposed velocities at the inlet and from the solved velocities at the outlet, by integrating the normal component. Eq. (31) is discretized through the same RBF-FD approach employed for the discretization of the Poisson Eq. (10) and solved using a direct LU decomposition.

The local Nusselt number Nu_y at the cold wall for the differentially heated cavity is obtained using the following expression:

$$\mathrm{Nu}_y = \frac{T_k - T_C}{1 - \hat{x}_k} \tag{32}$$

where k is the index of the internal node $\hat{\mathbf{x}}_k = \{\hat{x}_k, \hat{y}_k\}^T$ which is closest to the point $\mathbf{x} = \{1, y\}^T$ and T_k is its temperature. The mean Nusselt number $\overline{\mathrm{Nu}}$ on the cold wall is therefore given by $\overline{\mathrm{Nu}} = \int_0^1 \mathrm{Nu}_y \mathrm{d}y$.

The drag coefficient C_D for the case of the flow past a circular cylinder between parallel walls is defined as follows:

$$C_D = \frac{2F_x}{\rho_0 u_0^2 L d_{cyl}} \tag{33}$$

where F_x is the x-component of the force exerted by the fluid on the cylinder, which is time-averaged over a period $\bar{t}$ in the case of unsteady periodic flows.

4. Geometry and boundary conditions

The geometries for the problems are represented in Figure 2. The lid-driven cavity problem, Figure 2*a*, is defined by a square cavity with side length L where the top wall moves to the right with velocity u_0. The boundary conditions in terms of nondimensional variables are $\mathbf{u} = 0$ at $x = 0$, 1 and $y = 0$, $\mathbf{u} = \{1, 0\}^T$ at $y = 1$.

The differentially heated cavity problem, Figure 2*b*, is defined again by a square cavity with side length L where the horizontal walls are adiabatic while the vertical walls are isothermal. The temperature of the left wall (hot wall) is $T = T_H$ while the temperature of the right wall (cold wall) is $T_C < T_H$. The reference temperature for the buoyancy linearization is chosen to be the mean temperature $T_0 = (T_H + T_C)/2$ while the reference temperature scale is chosen to be $\Delta T = T_H - T_C$. The boundary conditions in terms of nondimensional variables are the following:

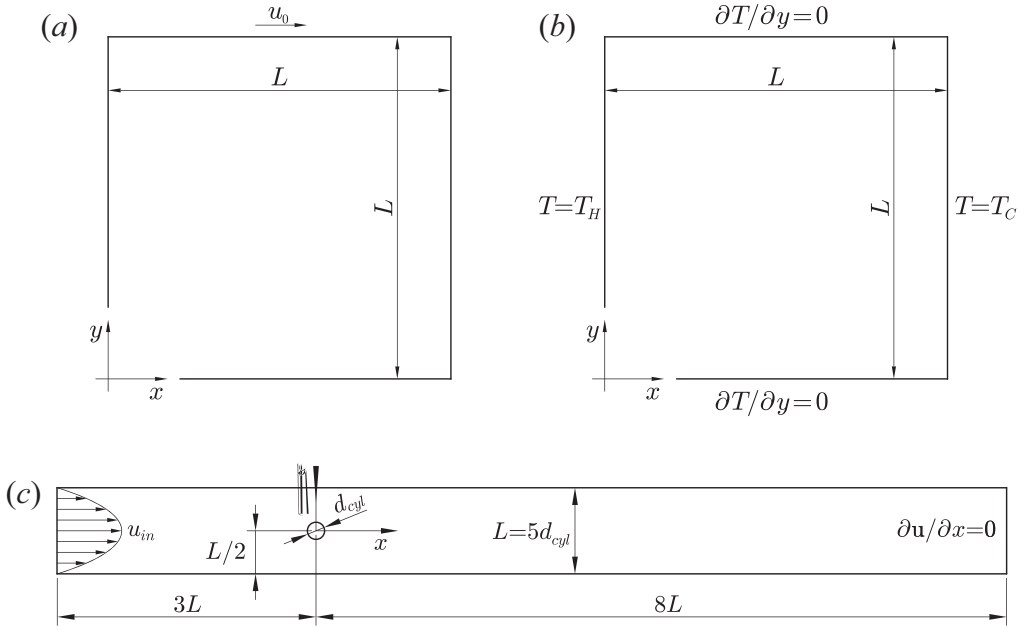

Figure 2. Geometries of the problems: (*a*) lid-driven cavity, (*b*) differentially heated cavity, (*c*) flow past a circular cylinder between parallel walls.

$$\begin{cases} \mathbf{u} = 0 & \text{at } x, y = 0, 1 \\ T = 1/2 & \text{at } x = 0 \\ T = -1/2 & \text{at } x = 1 \\ \dfrac{\partial T}{\partial y} = 0 & \text{at } y = 0, 1 \end{cases} \tag{34}$$

The problem of the flow past a circular cylinder between parallel walls, Figure 2*c*, is defined by a rectangular channel with height L and length $11\,L$ with a circular obstacle with diameter $d_{cyl} = L/5$ placed at half of the channel height and $3L = 15d_{cyl}$ downstream from the left inlet. The inlet velocity profile is parabolic with u_0 as mean value, while completely developed flow conditions are imposed at the outlet. The outlet is placed at $8L = 40d_{cyl}$ downstream from the cylinder in order to avoid any spurious influence of the outlet boundary conditions on the flow near the cylinder. The boundary conditions in terms of nondimensional variables are the following:

$$\begin{cases} \mathbf{u} = 0 & \text{at } y = -1/2, 1/2; \text{ on the cylinder} \\ \mathbf{u} = \left\{3/2{-}6y^2, 0\right\}^T & \text{at } x = -3 \\ \dfrac{\partial \mathbf{u}}{\partial x} = 0 & \text{at } x = 8 \end{cases} \tag{35}$$

5. Node distributions

The spacing function $s(x, y)$ employed for the lid-driven cavity problem is the following:

$$\frac{s(x,y)}{s_M} = \frac{1}{5} + \frac{1}{5}\left[1 + \cos\left(\pi(2x{-}1)^4\right)\right]\left[1 + \cos\left(\pi(2y{-}1)^4\right)\right] \tag{36}$$

for which the maximum spacing at the cavity center is s_M, while the minimum spacing at the walls is $s_m = s_M/5$ in order to accurately resolve the boundary layers. A graphical representation

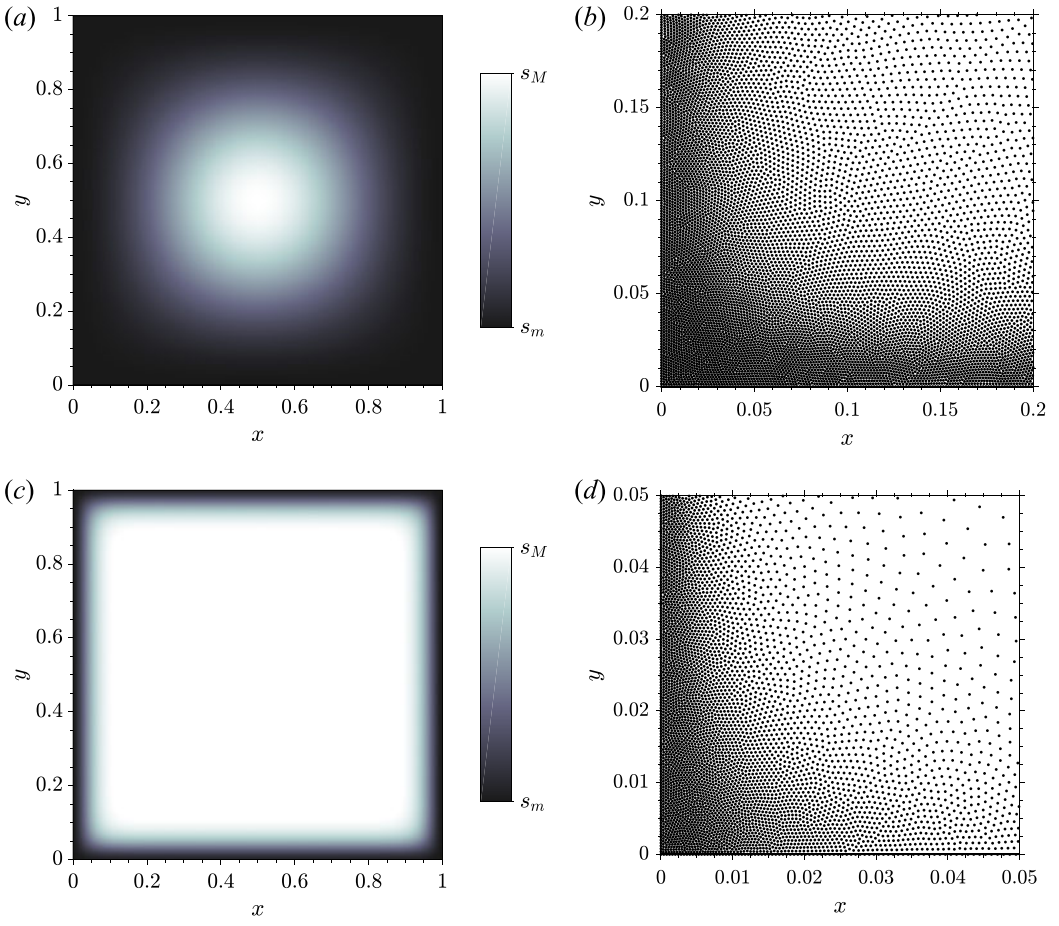

Figure 3. Spacing function (left) and enlarged view of the node distribution for the bottom left corner (right) with $N \approx 10^5$ nodes: (*a*, *b*) lid-driven cavity, (*c*, *d*) differentially heated cavity.

of the spacing function is given in Figure 3*a*, while Figure 3*b* shows an enlarged view of the node distribution for the bottom left corner in the case $N \approx 10^5$ nodes.

The spacing function $s(x, y)$ employed for the differentially heated cavity problem at $\mathrm{Ra}=10^6, 10^7$ and 10^8 is the following:

$$\frac{s(x,y)}{s_M} = \frac{1}{\gamma} + \frac{\gamma - 1}{4.2\gamma}\left[1 + \cos\left(\pi(2x-1)^8\right)\right]\left[1.1 + \cos\left(\pi(2y-1)^8\right)\right] \tag{37}$$

for which the maximum spacing at the cavity center is s_M and $\gamma = 40$. The minimum spacing at the vertical walls is $s_m = s_M/\gamma = s_M/40$, while the spacing at the horizontal walls is larger than s_m. This choice is motivated by the necessity of an accurate resolution of the thin boundary layers occurring at the isothermal vertical walls, especially for high Ra numbers. A graphical representation of the spacing function is given in Figure 3*c*, while Figure 3*d* shows an enlarged view of the node distribution for the bottom left corner.

The solutions of the differentially heated cavity at $\mathrm{Ra}=2 \times 10^8$ and 4×10^8, which are expected to be time-dependent, are obtained on highly stretched, nonuniform Cartesian node arrangements. This choice is due to the strong influence of the accurate resolution of the thin boundary layer on the time-dependent flow.

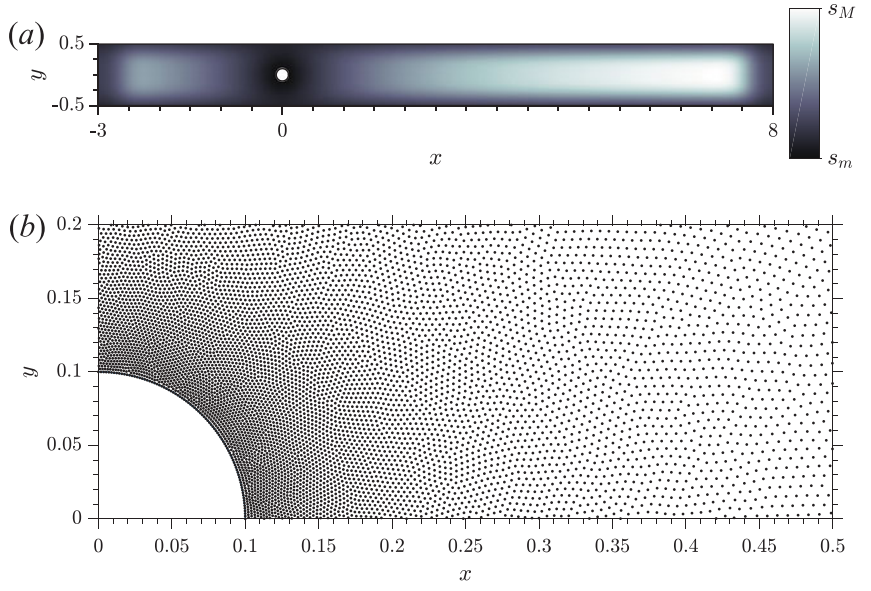

Figure 4. Spacing function (*a*) and enlarged view of the node distribution around the cylinder with $N\approx10^5$ nodes (*b*) for the flow past a circular cylinder between parallel walls.

The employed Cartesian coordinates of the nodes for both directions are:

$$\frac{x_i}{L}=\frac{i}{i_{MAX}}-\frac{1}{2\pi}\sin\left(\frac{2\pi i}{i_{MAX}}\right),\quad i=0,\ldots,i_{MAX} \tag{38}$$

as suggested in [44]. The spacing defined by Eq. (38) is extremely small at the walls: $2L\pi^2/(3i_{MAX}^3)$ orthogonally to the wall. Two Cartesian arrangements with $i_{MAX}=200$ ($N\approx40,000$ nodes) and $i_{MAX}=320$ ($N\approx100,000$ nodes) have been employed, for which the distance of the first node from the wall is 8.2×10^{-7} and 2.0×10^{-7} when $L=1$.

The spacing function $s(x, y)$ employed for the flow past a circular cylinder between parallel walls is defined as follows:

$$\frac{s(x,y)}{s_M}=\left[1+k_W\left(\frac{2y}{H}\right)^{2e_W}+k_C\frac{d_{cyl}}{2r}\right]^{-1} \tag{39}$$

where $k_W=3$, $e_W=1.75$, $k_C=24$, and $r=\sqrt{x^2+y^2}$ is the distance from the center of the cylinder. The ratio between the spacing at the channel walls and the maximum spacing s_M, encountered at the outlet, is approximately $1/(k_W+1)=1/4$, while the ratio between the spacing at the cylinder wall and the maximum spacing is approximately $1/(k_C+1)=1/25$. Again, a very small nodal spacing is employed near the cylinder in order to accurately resolve the boundary layers. A graphical representation of the spacing function is given in Figure 4*a*, while Figure 4*b* shows an enlarged view of the node distribution around the cylinder. A total number of nodes $N\approx10^5$ is employed for each test case in order to assess the properties of the proposed method with practical problem sizes.

6. Results

6.1. Lid-driven cavity

The lid-driven cavity problem has been solved for Reynolds numbers Re = 1,000, 5,000, and 7,500 with two different node distributions with $N\approx25,000$ nodes and $N\approx100,000$ nodes. The

Table 2. Comparison of streamfunction extrema for Re = 1,000, 5,000, 7,500

	Primary vortex, ψ (location)	Secondary vortex BR, ψ (location)	Secondary vortex BL, ψ (location)
Re = 1,000			
Present results			
$N \approx 2.5 \times 10^4$	−0.1188 (0.5237,0.5630)	1.700E − 3 (0.8668,0.1117)	2.270E − 4 (0.0837,0.0768)
$N \approx 10^5$	−0.1188 (0.5313,0.5686)	1.727E − 3 (0.8657,0.1141)	2.324E − 4 (0.0844,0.0775)
Bayona et al. [33]	−0.1189 (0.5308,0.5652)	1.730E − 3 (0.8641,0.1118)	2.334E − 4 (0.0832,0.0781)
Re = 5,000			
Present results			
$N \approx 2.5 \times 10^4$	−0.1162 (0.5222,0.5370)	2.863E − 3 (0.8036,0.0760)	1.264E − 3 (0.0759,0.1327)
$N \approx 10^5$	−0.1219 (0.5170,0.5354)	3.051E − 3 (0.8034,0.0726)	1.367E − 3 (0.0743,0.1370)
Bayona et al. [33]	−0.1223 (0.5151,0.5352)	3.077E − 3 (0.8046,0.0727)	1.379E − 3 (0.0728,0.1371)
Re = 7,500			
Present results			
$N \approx 2.5 \times 10^4$	−0.1177 (0.5074,0.5298)	3.044E − 3 (0.7907,0.0665)	1.397E − 3 (0.0679,0.1493)
$N \approx 10^5$	−0.1209 (0.5110,0.5326)	3.178E − 3 (0.7888,0.0646)	1.519E − 3 (0.0656,0.1506)
Bayona et al. [33]	−0.1230 (0.5132,0.5317)	3.241E − 3 (0.7909,0.0650)	1.553E − 3 (0.0642,0.1535)

BR = bottom right; BL = bottom left.

Table 3. Streamfunction values for lid-driven cavity streamline plots

-1×10^{-1}	-8×10^{-2}	-6×10^{-2}	-4×10^{-2}	-2×10^{-2}	-1×10^{-2}	-3×10^{-3}	-1×10^{-3}
-3×10^{-4}	-1×10^{-4}	-3×10^{-5}	-1×10^{-5}	-3×10^{-6}	-1×10^{-6}	-1×10^{-7}	-1×10^{-8}
-1×10^{-9}	-1×10^{-10}	-1×10^{-11}	-1×10^{-12}	-1×10^{-13}	-1×10^{-14}	0	1×10^{-14}
1×10^{-13}	1×10^{-12}	1×10^{-11}	1×10^{-10}	1×10^{-9}	1×10^{-8}	1×10^{-7}	1×10^{-6}
3×10^{-6}	1×10^{-5}	3×10^{-5}	1×10^{-4}	3×10^{-4}	1×10^{-3}	3×10^{-3}	1×10^{-2}

solution for Re = 10,000 is calculated using the fine distribution only, expecting a flow bifurcation between a steady solution at Re = 7,500 and a time-dependent, periodic solution for Re = 10,000, as suggested by different authors [45]–[47]. The calculation at Re = 1,000 is started from rest using a time step $\Delta t = 0.1$, reaching an asymptotic steady solution after an appropriate long time integration, i.e., over 200 time units. Steady solutions are also found for the cases Re = 5,000 and Re = 7,500 using a time step $\Delta t = 0.05$, starting from the steady solution at the Re value immediately below and integrating for over 400 time units. These steady solutions are in perfect agreement with the findings of Fortin et al. [46] and Bruneau and Saad [47], which predicted a critical Reynolds number $\mathrm{Re}_{cr} \approx 8,000$. The extrema of the streamfunction for the primary vortex at the center of the cavity and for the secondary vortices at bottom corners are reported in Table 2 for each of these cases, where the reference results of Bayona et al. [33] are also reported. Such reference results are obtained using a high order RBF-FD meshless approach with $n = 90$ local support nodes, $N \approx 40,000$ total nodes and a steady-state streamfunction formulation. Good agreement is found in each case, where the increase of the number of nodes from $N = 25,000$ to $N = 100,000$ suggests an apparently monotonic convergence towards the reference values. The streamlines at steady state for the streamfunction values reported in Table 3 are depicted in Figure 5 for Re = 1,000 and Re = 5,000, and in Figure 6 for Re = 7,500, with enlarged views of the corner regions. Such streamline figures agree, to graphical accuracy, to the ones reported in [33] and [45].

The calculation for Re = 10,000, performed on the fine node distribution, is started from the steady solution at Re = 7,500 using a time step $\Delta t = 0.05$, reaching an apparently periodic solution after about 1,000 time units. Such periodic behavior is deduced from the analysis of the time trace of the x-component of the velocity at the cavity center $x = y = 0.5$, reported in Figure 7. The frequency of the strongest harmonic component of this time trace is $f = 0.57$, which agrees with the reference value $f = 0.59$ reported in [45]. Good agreement with the same reference is also found for the mean value and the amplitude of this periodic signal. Streamfunction contours for the streamfunction values reported in Table 3 are reported in Figure 8 for four equally spaced time intervals along the main period $1/f$. From the analysis of Figure 8 it can be deduced that

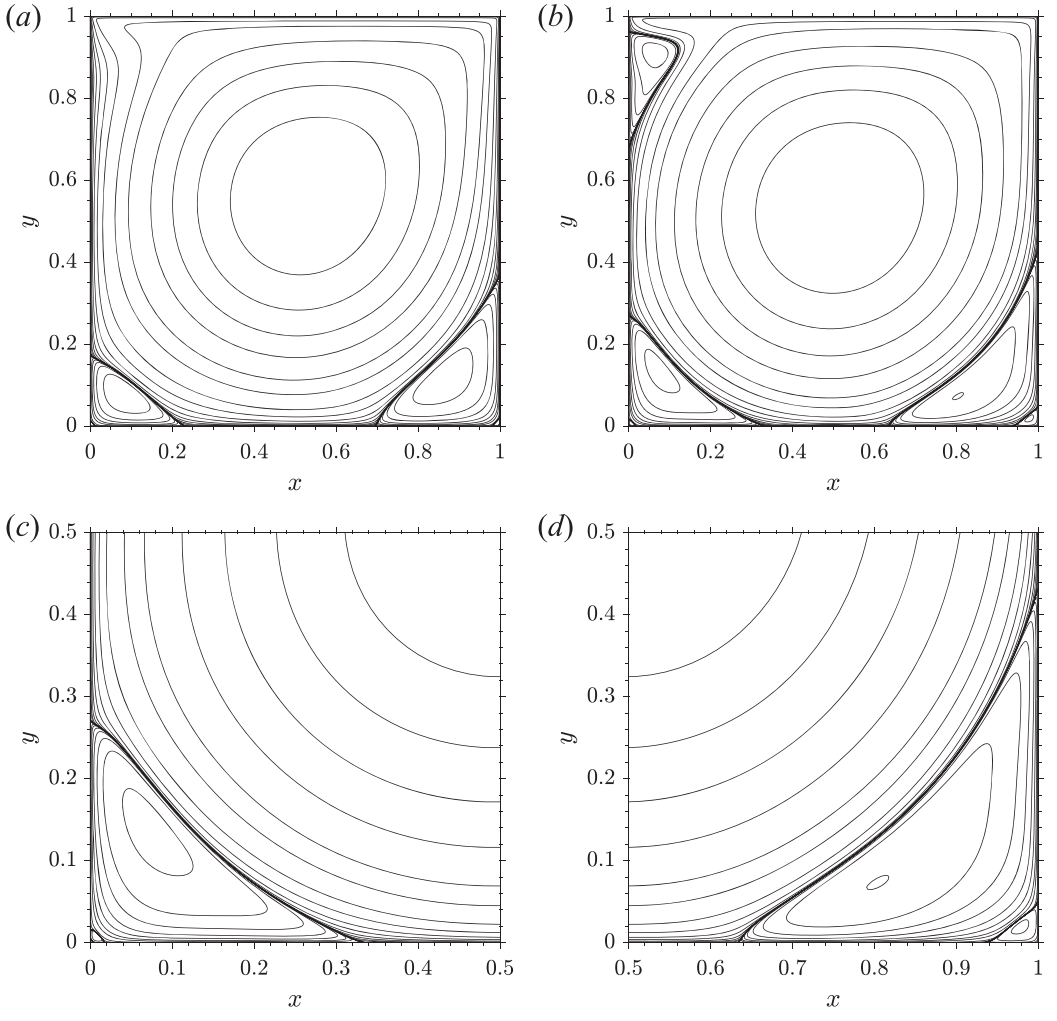

Figure 5. Streamfunction contours for Re = 1,000 (*a*), Re = 5,000 (*b*) with enlarged view of the bottom left (*c*) and bottom right (*d*) corners at Re = 5,000.

the time-dependent flow behavior is originated from the periodic growing and detaching of secondary and tertiary vortices from the bottom and left cavity walls. Again, the streamline plots agree, with graphical accuracy, to the ones reported in [45] for the same time instants.

6.2. Differentially heated cavity

The differentially heated cavity problem has been solved for Rayleigh numbers $\mathrm{Ra} = 10^6, 10^7, 10^8$ on an isotropic node distribution with $N \approx 10^5$ nodes, and for $\mathrm{Ra} = 2 \times 10^8, 4 \times 10^8$ on the stretched Cartesian node distributions with 200×200 and 320×320 nodes. A transition between a steady solution at $\mathrm{Ra} = 10^8$ and a time-dependent, periodic solution for $\mathrm{Ra} = 2 \times 10^8$ is expected, while the solution at $\mathrm{Ra} = 4 \times 10^8$ is expected to be weakly turbulent (chaotic), as suggested by different authors [44] and [48].

Starting from rest, a steady-state solution is found for $\mathrm{Ra} = 10^6$ after an appropriate long time integration for 300 time units using a time step $\Delta t = 0.1$. Steady solutions are also found for the cases $\mathrm{Ra} = 10^7$ and 10^8 using a time step $\Delta t = 0.05$, starting from the steady solution at the Ra

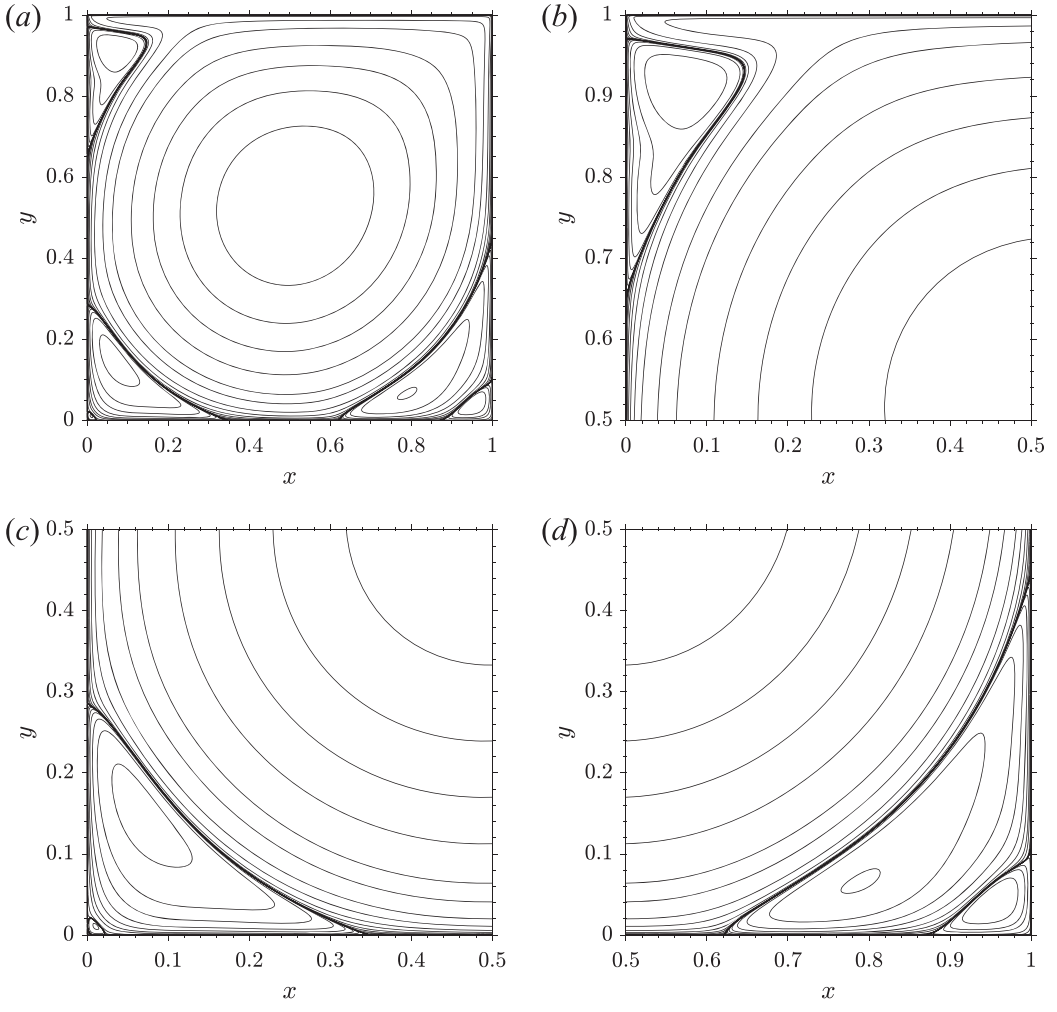

Figure 6. Streamfunction contours for Re = 7,500 (*a*), with enlarged view of the top left (*b*), bottom left (*c*), and bottom right (*d*) corners.

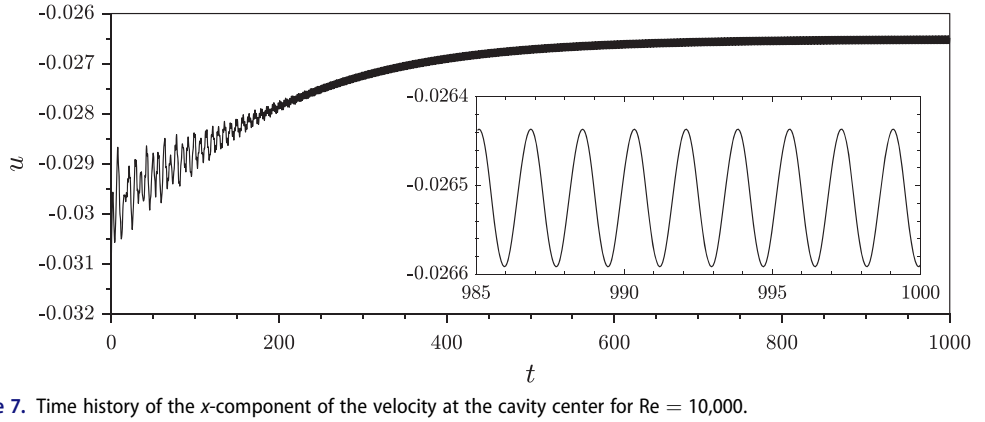

Figure 7. Time history of the *x*-component of the velocity at the cavity center for Re = 10,000.

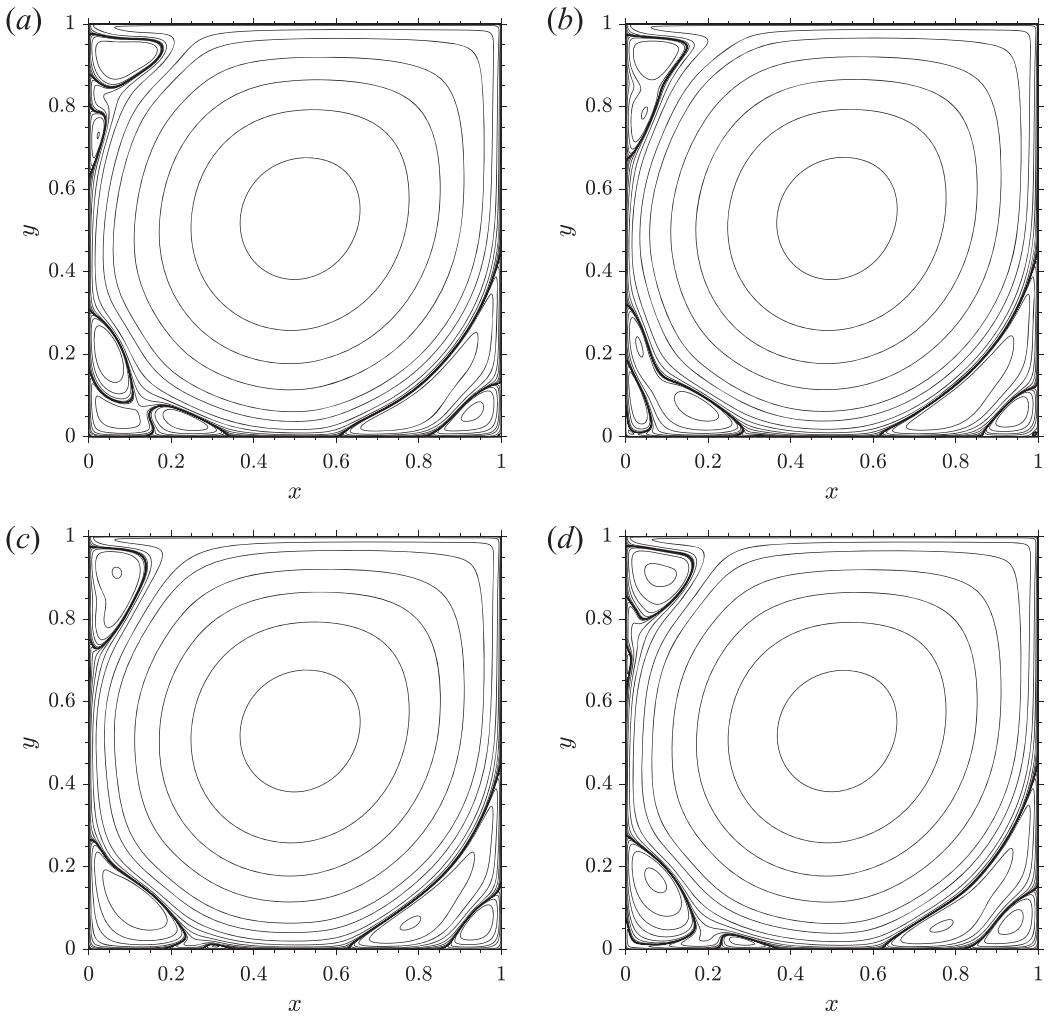

Figure 8. Streamfunction contours for Re = 10,000: (*a–d*) correspond to four equally spaced times along the main period $1/f = 1.75$.

value immediately below and integrating for more than 500 time units. These steady solutions are in perfect agreement with the findings of Janssen and Henkes [44] and Paolucci and Chenoweth [48], which predicted a critical Rayleigh number $Ra_{cr} \approx 1.93 \times 10^8$. Characteristic values such as mean, maximum, and minimum Nusselt number at the cold wall are reported in Table 4 for each of these cases, where the reference results of Contrino et al. [49] are also reported. Such reference results are obtained using a thermal lattice Boltzmann approach with fine meshes up to $2{,}043^2$. Very good agreement is found in each case, with slightly larger deviations from reference values only for $Ra = 10^8$. These deviations are probably due to the employed isotropic node distribution which is not refined enough to accurately solve the very thin boundary layers at the isothermal walls at such high Ra numbers.

Figure 9*a* depicts the local Nusselt number Nu_y at steady-state along the cold wall for the Ra numbers previously considered. The comparison with reference values from Contrino et al. [49] shows excellent agreement along the whole wall. The contour plots for streamfunction and temperature at steady state are reported in Figure 10, showing a very good agreement, to graphical accuracy, to the ones reported in [49] and [50].

Table 4. Comparison of characteristic values for the differentially heated cavity

	$\overline{Nu}$	Nu_{max}	y	Nu_{min}	y
$Ra = 10^6$					
Contrino et al. [49]	8.8252	17.5360	0.9608	0.9795	0.0006
Present results	8.8280	17.5611	0.9614	0.9793	0.0030
$Ra = 10^7$					
Contrino et al. [49]	16.5231	39.3950	0.9820	1.3659	0.0006
Present results	16.5159	39.3889	0.9818	1.3755	0.0022
$Ra = 10^8$					
Contrino et al. [49]	30.2251	87.2454	0.9917	1.9195	0.0010
Present results	30.0887	86.7845	0.9914	1.9694	0.0014

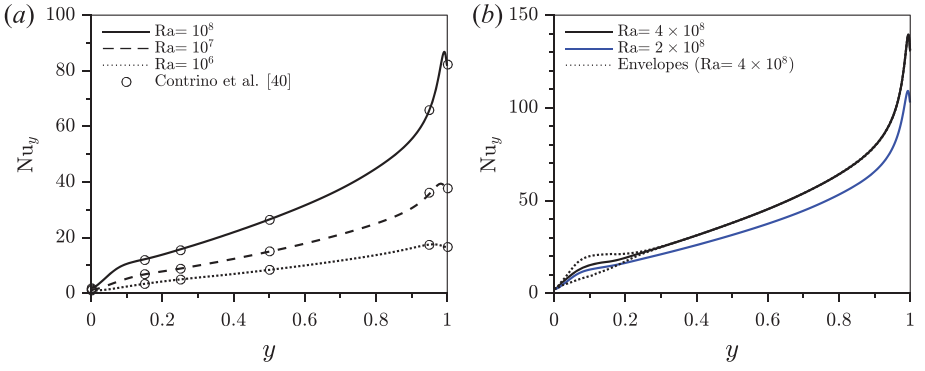

Figure 9. Local Nusselt number Nu_y along the cold wall for (*a*) steady-state solutions and (*b*) time-dependent solutions (time averaged).

The case $Ra = 2 \times 10^8$, which is a slightly larger Ra number than the critical value $Ra_{cr} \approx 1.93 \times 10^8$, is started from the computed steady solution at $Ra = 10^8$ which is interpolated onto the 200×200 Cartesian node distribution. After an integration over 300 time units using a time step $\Delta t = 0.03$, an apparently periodic solution is found, albeit not completely developed. The periodic behavior is deduced from the analysis of the time trace of the temperature for the node which is closest to the point $(0.1032, 0.8036)$, suggested in [48], and is reported in Figure 11*a*. In order to investigate the influence of the node distribution on the time dependent solution at this Ra number, the calculated solution is interpolated onto the fine 320^2 Cartesian node distribution for a successive integration over 300 additional time units with the same time step $\Delta t = 0.03$. The analysis of time trace of the temperature at the same point $(0.1032, 0.8036)$ is reported in Figure 11*b* and confirms the periodic behavior calculated with the coarse distribution. The frequency $f = 0.0532$ of the strongest component is in close agreement with the value $f = 0.0527$ obtained by Janssen and Henkes [44] with a fourth order finite volume scheme and a 360^2 grid. The time trace also reveals a small harmonic component with frequency $2f = 0.1064$ and the presence of a low-frequency component whose frequency is estimated to be $f' \approx 0.008$, which is also in good agreement with the value $f' = 0.0078$ obtained by Janssen and Henkes. They also showed that this low-frequency component is damped and has a very slow decay, requiring long integration periods to be eliminated, e.g., 3,000 time units.

The solution at $Ra = 4 \times 10^8$ is calculated on the fine distribution only, starting from the last available solution at $Ra = 2 \times 10^8$ and integrating for 300 time units with $\Delta t = 0.02$. The time trace of the temperature at the point $(0.1032, 0.8036)$ is reported in Figure 12, from which it can be observed that the solution cannot be described by a limited number of harmonic components and the flow is described as chaotic or weakly turbulent [48]. This chaotic behavior agrees with the findings of Paolucci and Chenoweth [48] which performed calculations for the same Ra number using a finite difference scheme on a 121^2 grid.

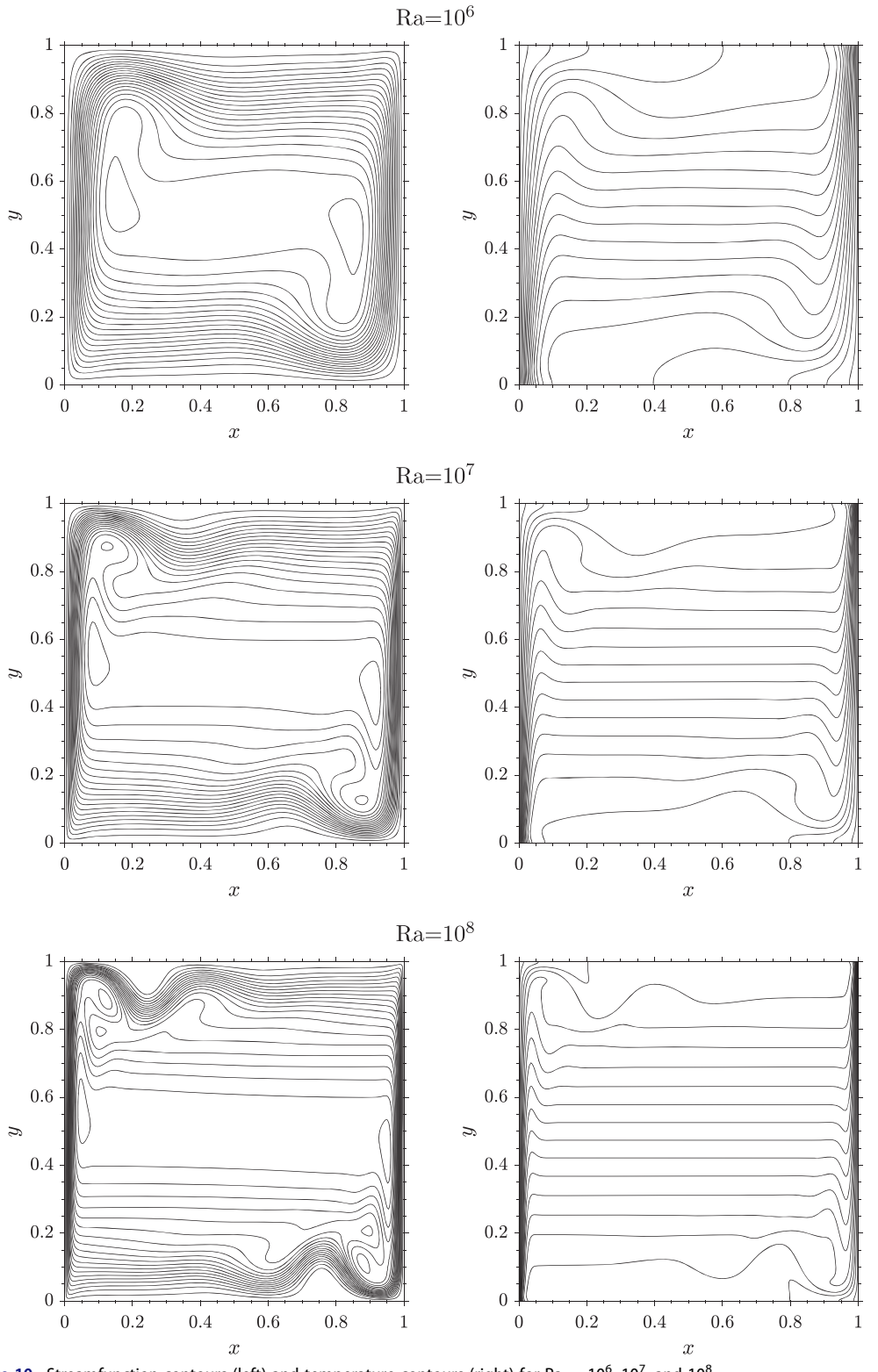

Figure 10. Streamfunction contours (left) and temperature contours (right) for Ra $= 10^6$, 10^7, and 10^8.

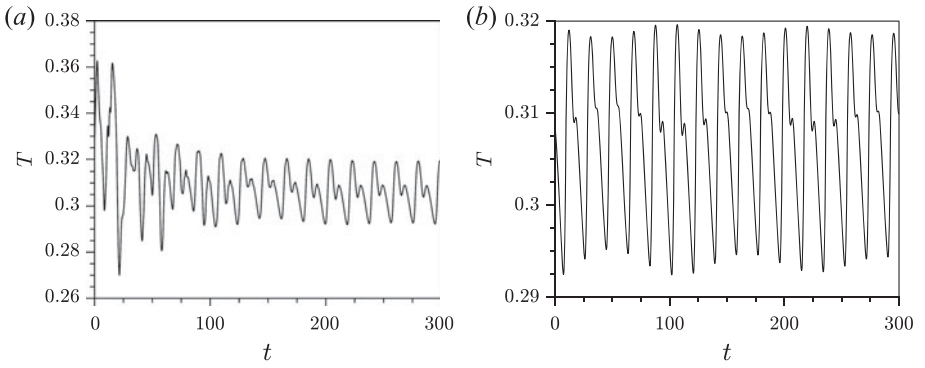

Figure 11. Time traces of the temperature at point (0.1032,0.8036) for Ra=2×10^8 using (*a*) 200×200 and (*b*) 320×320 highly stretched Cartesian grids.

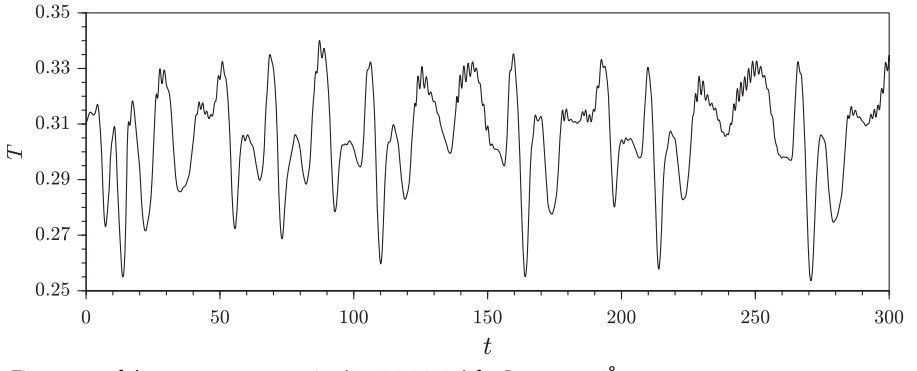

Figure 12. Time trace of the temperature at point (0.1032,0.8036) for Ra $= 4 \times 10^8$.

Table 5. Time steps Δt at different Re number for the flow past a cylinder

Re	200	300	500	1,000	2,000	4,000	8,000
Δt	0.025	0.020	0.015	0.015	0.015	0.010	0.010

Table 6. Comparison of nondimensional period $\bar{t}$ and time-averaged drag coefficient C_D

	Re	200	300	500	1,000	2,000	4,000	8,000
Present results	$\bar{t}$	–	0.80	0.72	0.65	0.60	0.56	0.52
	C_D	3.41	2.99	2.77	2.74	2.79	2.79	2.78
Zovatto and Pedrizzetti [52]	$\bar{t}$	–	0.81	0.73	0.67	–	–	–
	C_D	3.40	2.94	2.68	2.62	–	–	–

Figure 9*b* shows the time averaged local Nusselt number Nu_y along the cold wall for Ra= 2×10^8 and 4×10^8. The envelopes for the highest Ra value are also shown, highlighting the activity at the bottom of the cold wall.

6.3. Flow past a circular cylinder between parallel walls

The case of the flow past a circular cylinder between parallel walls has been solved for Reynolds numbers Re = 200, 300, 500, 1,000, 2,000, 4,000, and 8,000, expecting a time-dependent flow for the cases Re≥300, as suggested by different authors [51] and [52]. The calculation at Re = 200 is started from rest using a time step $\Delta t = 0.025$, reaching an asymptotic steady solution after an

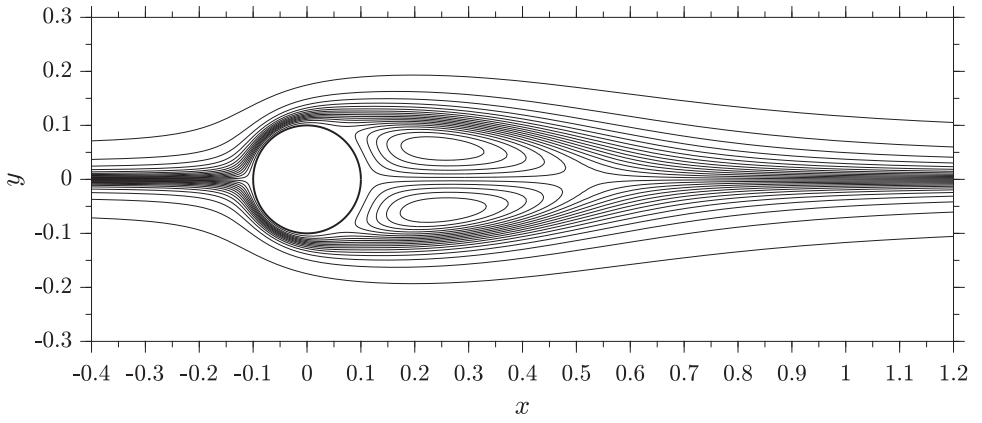

Figure 13. Streamlines for the steady flow at Re = 200.

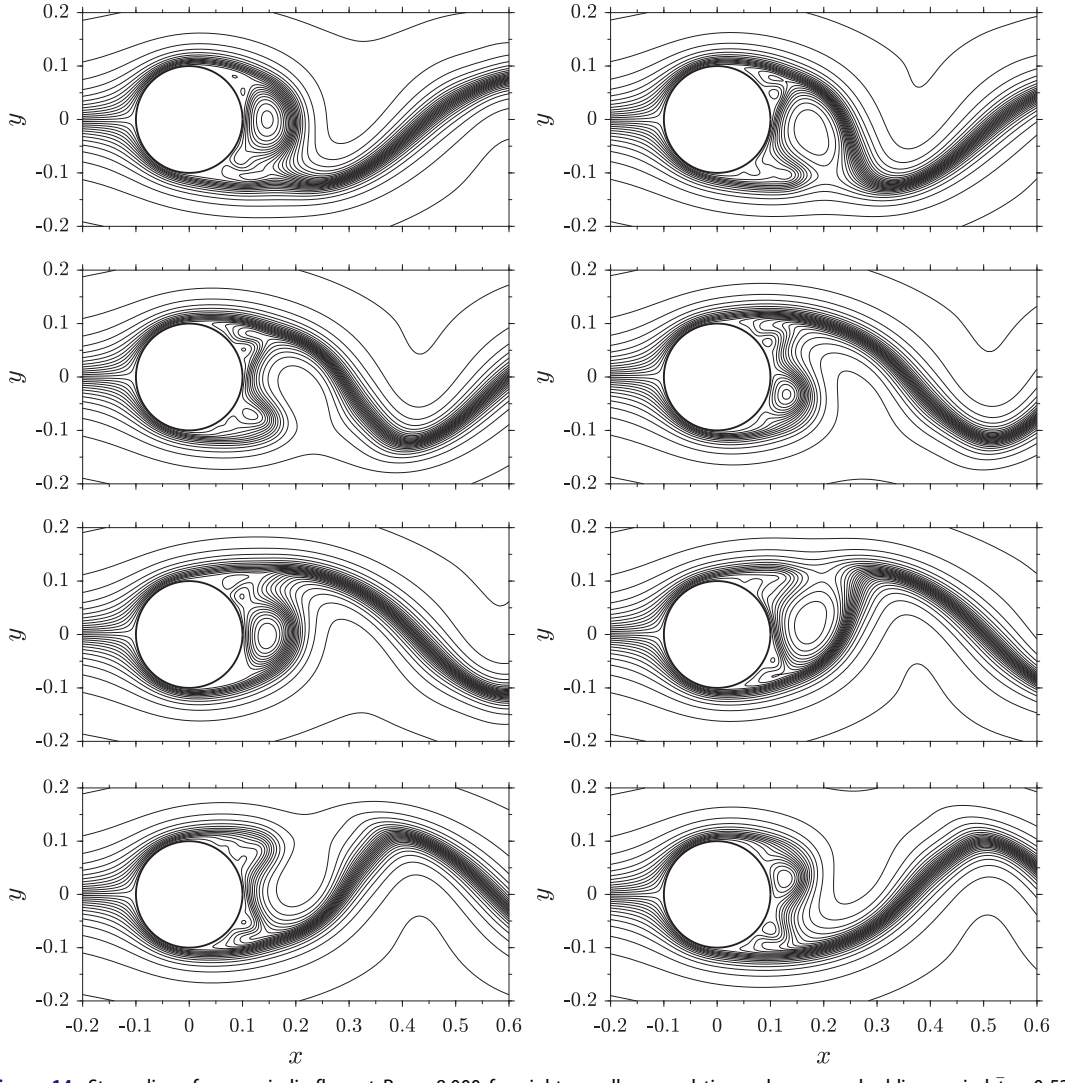

Figure 14. Streamlines for a periodic flow at Re = 8,000 for eight equally spaced times along one shedding period $\bar{t} = 0.52$ (left to right, top to bottom).

appropriate time integration for over 100 time units. Periodic solutions are found in the remaining cases, using the time steps reported in Table 5, starting from the solution at the Re value immediately below and integrating for over 200 time units for each case. These periodic solutions are in perfect agreement with the findings of Zovatto and Pedrizzetti [52] and Chen et al. [51], which predicted a critical Reynolds number $Re_{cr} \approx 231$. The periodic flow is due to the onset of an unsteady periodic shedding regime in the cylinder wake. The values of the nondimensional shedding period $\bar{t}$ and drag coefficient C_D are reported in Table 6, where the reference results of Zovatto and Pedrizzetti [52] are also reported. Good agreement for both $\bar{t}$ and C_D is found for low Re numbers, while slightly larger deviations of C_D are found for higher Re. The calculations for Re $>$ 1,000 are carried out mainly for the purpose of showing the stability of the proposed method for high Re numbers, for which more accurate solutions require the use of more nodes.

A streamline plot for the steady solution at Re $=$ 200 is reported in Figure 13, which shows the typical recirculating zones with perfect symmetry behind the cylinder. Streamfunction contours for the case Re $=$ 8,000 are reported in Figure 14 for eight equally spaced time instants along one shedding period $\bar{t} = 0.52$. Although the computed solution at such high Re is not claimed to be accurate, these figures shows that the proposed method can deal with high Re numbers without the appearance of any long time integration instability or spurious effect, therefore enabling the possibility to face engineering relevant problems.

7. Conclusions

In this work a RBF-FD meshless approach is used for the numerical simulation of unsteady fluid flow problems with heat transfer using primitive variables, i.e., velocity and pressure, on general-shaped 2D domains with node distributions of practical relevance. A projection scheme is employed to decouple the momentum and continuity equation, while an implicit scheme is employed for the solution of the momentum and energy equations. Such solution strategy is proven to be effective in the long time integration of unsteady flows with large time steps. The lid-driven cavity, the differentially heated cavity and the flow past a circular cylinder between parallel walls have been chosen as test cases to assess the properties of the presented numerical approach. Several computations for moderately high and high Reynolds (Re) and Rayleigh (Ra) numbers are carried out in order to validate the effectiveness and accuracy of the proposed meshless approach at different flow regimes, from steady state to periodical time-dependent flows.

The obtained numerical results agree very favorably with literature references for moderately high Re or Ra numbers, while the accurate solution for the higher Re or Ra cases requires the use of more nodes than those employed in this work, i.e., $N \gg 10^5$ nodes. This is not a problem since the proposed scheme is intended to deal with large size problems of practical interest, and it is proven to be computationally efficient. Such favorable results suggest that the proposed meshless strategy can be effectively employed for the efficient numerical simulation of unsteady fluid flow problems with heat transfer on complex-shaped 2D domains with arbitrary node distributions of practical engineering relevance, including highly anisotropic node distributions. This approach can also be extended to 3D problems with remarkable geometrical advantages over standard mesh-based methods. The extension to more complex model problems, e.g., turbulence models, is also straightforward.

References

[1] G. Liu, *Meshfree Methods: Moving beyond the Finite Element Method*. Boca Raton, FL: CRC Press, 2009.

[2] H. Li and S. Mulay, *Meshless Methods and Their Numerical Properties*. Boca Raton, FL: CRC Press, 2013.

[3] G. Fasshauer, "Solving partial differential equations by collocation with radial basis functions," presented at the Proceedings of the 3rd International Conference on Curves and Surfaces, Chamonix-Mont-Blanc, 1996.

[4] C. Franke and R. Schaback, "Solving partial differential equations by collocation using radial basis functions," *Appl. Math. Comput.*, vol. 93, no. 1, pp. 73–82, 1998. DOI: 10.1016/S0096-3003(97)10104-7.
[5] M. Golberg, C. Chen, and H. Bowman, "Some recent results and proposals for the use of radial basis functions in the BEM," *Eng. Anal. Bound. Elem.*, vol. 23, no. 4, pp. 285–296, 1999. DOI: 10.1016/S0955-7997(98)00087-3.
[6] E. Larsson and B. Fornberg, "A numerical study of some radial basis function based solution methods for elliptic PDEs," *Comput. Math. Appl.*, vol. 46, no. 5, pp. 891–902, 2003. DOI: 10.1016/S0898-1221(03)90151-9.
[7] S. Sarra and E. Kansa, "Multiquadric radial basis function approximation methods for the numerical solution of partial differential equations," *Adv. Comput. Mech.*, vol. 2, pp. 1–206, 2009.
[8] B. Fornberg and N. Flyer, "Solving PDEs with radial basis functions," *Acta Numer.*, vol. 24, pp. 215–258, 2015. DOI: 10.1017/S0962492914000130.
[9] M. Li, C. S. Chen, and C. H. Tsai, "Meshless method based on radial basis functions for solving parabolic partial differential equations with variable coefficients," *Numer. Heat Transfer B Fund.*, vol. 57, no. 5, pp. 333–347, 2010. DOI: 10.1080/10407790.2010.481489.
[10] E. Kansa, "Multiquadrics—A scattered data approximation scheme with applications to computational fluid-dynamics—II solutions to parabolic, hyperbolic and elliptic partial differential equations," *Comput. Math. Appl.*, vol. 19, no. 8, pp. 147–161, 1990. DOI: 10.1016/0898-1221(90)90271-K.
[11] C. Lee, X. Liu, and S. Fan, "Local multiquadric approximation for solving boundary value problems," *Comput. Mech.*, vol. 30, no. 5, pp. 396–409, 2003. DOI: 10.1007/s00466-003-0416-5.
[12] B. Šarler and R. Vertnik, "Meshfree explicit local radial basis function collocation method for diffusion problems," *Comput. Math. Appl.*, vol. 51, no. 8, pp. 1269–1282, 2006. DOI: 10.1016/j.camwa.2006.04.013.
[13] G. Chandhini and Y. Sanyasiraju, "Local RBF-FD solutions for steady convection-diffusion problems," *Int. J. Numer. Meth. Eng.*, vol. 72, no. 3, pp. 352–378, 2007. DOI: 10.1002/nme.2024.
[14] E. Divo and A. J. Kassab, "Localized meshless modeling of Natural-Convective viscous flows," *Numer. Heat Transfer B Fund.*, vol. 53, no. 6, pp. 487–509, 2008. DOI: 10.1080/10407790802083190.
[15] J. Sun, H.-L. Yi, and H.-P. Tan, "Local RBF meshless scheme for coupled radiative and conductive heat transfer," *Numer. Heat Transfer A Appl.*, vol. 69, no. 12, pp. 1390–1404, 2016. DOI: 10.1080/10407782.2016.1139959.
[16] T. T. V. Le, N. Mai-Duy, K. Le-Cao, and T. Tran-Cong, "A time discretization scheme based on integrated radial basis functions for heat transfer and fluid flow problems," *Numer. Heat Transfer B Fund.*, vol. 74, no. 2, pp. 498–518, 2018. DOI: 10.1080/10407790.2018.1515329.
[17] K. Le-Cao, N. Mai-Duy, and T. Tran-Cong, "An effective integrated-RBFN Cartesian-grid discretization for the stream functionvorticitytemperature formulation in nonrectangular domains," *Numer. Heat Transfer B Fund.*, vol. 55, no. 6, pp. 480–502, 2009. DOI: 10.1080/10407790902827470.
[18] M. Q. Wang, C. X. Wang, M. Li, and C. S. Chen, "A numerical scheme based on FD-RBF to solve Fractional-Diffusion inverse heat conduction problems," Numer. Heat *Transfer A Appl.*, vol. 68, no. 9, pp. 978–992, 2015. DOI: 10.1080/10407782.2014.986376.
[19] N. Li, Z. Tan, and X. Feng, "Novel two-level discretization method for high dimensional semilinear elliptic problems base on RBF-FD scheme," Numer *Heat Transfer B Fund.*, vol. 72, no. 5, pp. 349–360, 2017.
[20] G. Wright and B. Fornberg, "Scattered node compact finite difference-type formulas generated from radial basis functions," *J. Comput. Phys.*, vol. 212, no. 1, pp. 99–123, 2006. DOI: 10.1016/j.jcp.2005.05.030.
[21] B. Šarler, "From global to local radial basis function collocation method for transport phenomena," in *Computational Methods in Applied Sciences*, V. Leitão, C. Alves, and C. Duarte, Eds. Springer: Dordrecht, The Netherlands, 2007. *Adv. Meshfree Tech.*, vol. 5, pp. 257–282, 2007.
[22] G. Yao, Siraj-Ul-Islam, and B. Šarler, "Assessment of global and local meshless methods based on collocation with radial basis functions for parabolic partial differential equations in three dimensions," *Eng. Anal. Bound. Elem*, vol. 36, no. 11, pp. 1640–1648, 2015.
[23] J. Waters, and D. Pepper, "Global versus localized RBF meshless methods for solving incompressible fluid flow with heat transfer," *Numer. Heat Transfer B Fund.*, vol. 68, no. 3, pp. 185–203, 2015. DOI: 10.1080/10407790.2015.1021590.
[24] E. Divo and A. Kassab, "An efficient localized radial basis function meshless method for fluid flow and conjugate heat transfer," *J. Heat Transfer*, vol. 129, no. 2, pp. 124–136, 2007. DOI: 10.1115/1.2402181.
[25] G. Kosec and B. Šarler, "Solution of thermo-fluid problems by collocation with local pressure correction," *Int. J. Numer. Methods Heat Fluid Flow*, vol. 18, no. 7/8, pp. 868–882, 2008. DOI: 10.1108/09615530810898999.
[26] P. Chinchapatnam, K. Djidjeli, P. Nair, and M. Tan, "A compact RBF-FD based meshless method for the incompressible Navier-Stokes equations," presented at the *Proceedings of the IMechE, Part M. J. Eng. Maritime Environ.*, vol. 223, no. 3, pp. 275–290, 2009. DOI: 10.1243/14750902JEME151.

[27] G. Kosec, and B. Šarler, "Solution of a low prandtl number natural convection benchmark by a local meshless method," *Int. J. Numer. Methods Heat Fluid Flow*, vol. 23, no. 1, pp. 189–204, 2013. DOI: 10.1108/09615531311289187.
[28] Z. Wang, Z. Huang, W. Zhang, and G. Xi, "A meshless local radial basis function method for two-dimensional incompressible Navier-Stokes equations," *Numer. Heat Transfer B Fund.*, vol. 67, no. 4, pp. 320–337, 2015. DOI: 10.1080/10407790.2014.955779.
[29] A. Chorin, "Numerical solution of the Navier-Stokes equations," *Math. Comput.*, vol. 22, no. 104, pp. 745–762, 1968. DOI: 10.1090/S0025-5718-1968-0242392-2.
[30] R. Zamolo, and E. Nobile, "Two algorithms for fast 2D node generation: Application to RBF meshless discretization of diffusion problems and image halftoning," *Comput. Math. Appl.*, vol. 75, no. 12, pp. 4305–4321, 2018. DOI: 10.1016/j.camwa.2018.03.031.
[31] R. Finkel and J. Bentley, "Quad trees a data structure for retrieval on composite keys," *Acta Inform.*, vol. 4, no. 1, pp. 1–9, 1974. DOI: 10.1007/BF00288933.
[32] R. Floyd and L. Steinberg, "An adaptive algorithm for spatial greyscale," *Proc. Soc. Inform. Display*, vol. 17, no. 2, pp. 75–77, 1976.
[33] V. Bayona, N. Flyer, B. Fornberg, and G. Barnett, "On the role of polynomials in RBF-FD approximations: II. Numerical solution of elliptic PDEs," *J. Comput. Phys.*, vol. 332, pp. 257–273, 2017. DOI: 10.1016/j.jcp.2016.12.008.
[34] R. Hardy, "Multiquadric equations of topography and other irregular surfaces," *J. Geophys. Res.*, vol. 76, no. 8, pp. 1905–1915, 1971. DOI: 10.1029/JB076i008p01905.
[35] R. Franke, "A Critical Comparison of Some Methods for Interpolation of Scattered Data (Technical Report)," Monterey, CA: Naval Postgraduate School, Technical Report NPS-53-79-003, 1980.
[36] R. Franke, "Scattered data interpolation: tests of some methods," *Math. Comput.*, vol. 38, no. 157, pp. 181–200, 1982. DOI: 10.1090/S0025-5718-1982-0637296-4.
[37] N. Flyer, B. Fornberg, V. Bayona, and G. Barnett, "On the role of polynomials in RBF-FD approximations: I. Interpolation and accuracy," *J. Comput. Phys.*, vol. 321, pp. 21–38, 2016. DOI: 10.1016/j.jcp.2016.05.026.
[38] G. Fasshauer, "Meshfree approximation methods with Matlab," in *Interdisciplinary Mathematical Sciences*, vol. 6, ch. 9: *Conditionally Positive Definite Radial Functions*. Singapore: World Scientific, 2007.
[39] R. Horn, and C. Johnson, *Matrix Analysis*. Cambridge, UK: Cambridge University Press, 1990.
[40] S. Armfield, "Finite difference solutions of the Navier-Stokes equations on staggered and non-staggered grids," *Comput. Fluids*, vol. 20, no. 1, pp. 1–17, 1991. DOI: 10.1016/0045-7930(91)90023-B.
[41] H. van der Vorst, "Bi-CGSTAB: A fast and smoothly converging variant of Bi-CG for the solution of nonsymmetric linear systems," *SIAM J. Sci. Stat. Comp.*, vol. 13, no. 2, pp. 631–644, 1992. DOI: 10.1137/0913035.
[42] Y. Saad, "Iterative methods for sparse linear systems," in *Preconditioning Techniques*, 2nd ed., ch. 10. Philadelphia, PA: SIAM, 2003.
[43] E. Cuthill, and J. McKee, "Reducing the bandwidth of sparse symmetric matrices," in *Proceedings of the 1969 24th National Conference*, ACM '69. New York, NY: ACM, pp. 157–172, 1969.
[44] R. J. A. Janssen, and R. A. W. M. Henkes, "Accuracy of finite-volume discretizations for the bifurcating natural-convection flow in a square cavity," *Numer Heat Transfer B Fund.*, vol. 24, no. 2, pp. 191–207, 1993. DOI: 10.1080/10407799308955889.
[45] E. Nobile, "Simulation of time-dependent flow in cavities with the additive-correction multigrid method, part II: applications," *Numer Heat Transfer B Fund.*, vol. 30, no. 3, pp. 351–370, 1996. DOI: 10.1080/10407799608915087.
[46] A. Fortin, M. Jardak, J. Gervais, and R. Pierre, "Localization of hopf bifurcations in fluid flow problems," *Int. J. Numer. Methods Fluids*, vol. 24, no. 11, pp. 1185–1210, 1997. DOI: 10.1002/(SICI)1097-0363(19970615)24:11<1185::AID-FLD535>3.3.CO;2-O.
[47] C.-H. Bruneau and M. Saad, "The 2D lid-driven cavity problem revisited," *Comput. Fluids*, vol. 35, no. 3, pp. 326–348, 2006. DOI: 10.1016/j.compfluid.2004.12.004.
[48] S. Paolucci and D. R. Chenoweth, "Transition to chaos in a differentially heated vertical cavity," *J. Fluid Mech.*, vol. 201, no. 1, pp. 379, 1989. DOI: 10.1017/S0022112089000984.
[49] D. Contrino, P. Lallemand, P. Asinari, and L.-S. Luo, "Lattice-Boltzmann simulations of the thermally driven 2D square cavity at high Rayleigh numbers," *J. Comput. Phys.*, vol. 275, pp. 257–272, 2014. DOI: 10.1016/j.jcp.2014.06.047.
[50] P. Le Quéré, "Accurate solutions to the square thermally driven cavity at high rayleigh number," *Comput. Fluids*, vol. 20, no. 1, pp. 29–41, 1991. DOI: 10.1016/0045-7930(91)90025-D.
[51] J.-H. Chen, W. G. Pritchard, and S. J. Tavener, "Bifurcation for flow past a cylinder between parallel planes," *J. Fluid Mech.*, vol. 284, no. 1, pp. 23–41, 1995. DOI: 10.1017/S0022112095000255.
[52] L. Zovatto and G. Pedrizzetti, "Flow about a circular cylinder between parallel walls," *J. Fluid Mech.*, vol. 440, pp. 1–25, 2001.